Assessment of Sm^{2+}-doped SrI_2, EuI_2, and YbI_2 for near-infrared scintillator applications

van Aarle, Casper; Biner, Daniel A.; Krämer, Karl W.; Dorenbos, Pieter

DOI
10.1016/j.optmat.2024.116583

Publication date
2025

Document Version
Final published version

Published in
Optical Materials

Citation (APA)
van Aarle, C., Biner, D. A., Krämer, K. W., & Dorenbos, P. (2025). Assessment of Sm^{2+}-doped SrI_2, EuI_2, and YbI_2 for near-infrared scintillator applications. *Optical Materials*, *162*, Article 116583. https://doi.org/10.1016/j.optmat.2024.116583

Optical Materials 162 (2025) 116583

Contents lists available at ScienceDirect

Optical Materials

journal homepage: www.elsevier.com/locate/optmat

Assessment of Sm^{2+}-doped SrI_2, EuI_2, and YbI_2 for near-infrared scintillator applications

Casper van Aarle [a,*], Daniel A. Biner [b], Karl W. Krämer [b], Pieter Dorenbos [a]

[a] Faculty of Applied Sciences, Delft University of Technology, Mekelweg 15, Delft, The Netherlands
[b] Department of Chemistry, Biochemistry and Pharmaceutical Sciences, University of Bern, Freiestrasse 3, Bern, Switzerland

ARTICLE INFO

Keywords:
Scintillation
Near-infrared
Samarium
Single crystals
Self-absorption
Lanthanides

ABSTRACT

SrI_2:Eu^{2+} and CaI_2:Eu^{2+} are two of the brightest known scintillators, but they both suffer from self-absorption. Their respective undoped isostructural compounds EuI_2 and YbI_2 are not suitable for scintillation due to the additional problem of concentration quenching. These compounds can however be doped with Sm^{2+} to turn them into near-infrared emitting scintillators, with the additional benefit that the self-absorption probability of the Sm^{2+} emission is low. Here, the scintillation properties of SrI_2:1%Sm^{2+}, EuI_2:4%Sm^{2+}, and YbI_2:1%Sm^{2+} single crystals are assessed which were grown by the vertical Bridgman technique. SrI_2:1%Sm^{2+} and EuI_2:4%Sm^{2+} fall within the ideal wavelength range for detection with silicon based photodetectors and are spectroscopically very similar to each other. However, the key difference is that the scintillation decay time of EuI_2:4%Sm^{2+} is 1.1 μs, much shorter than the 1.8 μs of SrI_2:1%Sm^{2+}. Both SrI_2:Sm^{2+} and EuI_2:Sm^{2+} are identified as interesting candidates for further optimisation in the development of near-infrared emitting scintillators.

1. Introduction

Scintillation research between Delft University of Technology in The Netherlands and the University of Bern in Switzerland has a very long history that started already in 1992 and is still active today. The focus in the TU-Delft laboratories was always on the scintillator characterisation and the fundamental aspects of scintillation and scintillation mechanisms. The group in Bern, headed until his retirement in 2006 by prof. H. U. Güdel, was specialised in the synthesis of halide (chloride, bromide, iodide) single crystals activated with lanthanide luminescence centers. The collaboration has resulted in the discovery of excellent new scintillation materials, e.g., Cs_2LiYCl_6:Ce^{3+} in 1999 [1], $LaCl_3$:Ce^{3+} in 2000 [2], $LaBr_3$:Ce^{3+} in 2001 [3]. The already excellent properties of $LaBr_3$:Ce^{3+} were further improved in 2013 by means of Sr^{2+} co-doping [4]. Many other halide crystals activated with Ce^{3+} were explored over the years, and since the fundamental limits on scintillation performance were thought to have been reached the focus was shifted to near-infrared (NIR) scintillating materials based on Sm^{2+} activation. A first proof of principle was provided with SrI_2:Eu^{2+},Sm^{2+} and $CsBa_2I_5$: Eu^{2+},Sm^{2+} in 2019 [5,6].

SrI_2 and $CsBa_2I_5$ were selected as host materials for this proof of principle, because they form some of the brightest scintillator materials when doped with Eu^{2+}. Undoped SrI_2 already shows efficient host exciton emission with a light yield of 33,000 ph/MeV [7]. When doping SrI_2 with Eu^{2+}, the exciton emission intensity decreases and is replaced by Eu^{2+} $4f^65d \rightarrow 4f^7$ emission [8]. Increasing the Eu^{2+} concentration from 0% to 5% also increases the light yield to a value in excess of 80,000 ph/MeV [9–13].

The main problem of SrI_2:Eu^{2+} is self-absorption, where a photon emitted by Eu^{2+} gets reabsorbed by another Eu^{2+} ion before it exits the crystal. To illustrate why this occurs, Fig. 1a shows the energy levels of Eu^{2+} in the band gap of SrI_2 on a vacuum referred binding energy (VRBE) scale. The diagram is constructed with the parameters published in [14]. The $4f^65d \rightarrow 4f^7$ transition of Eu^{2+} only has the $4f^7$ ground state as final state, which is the same state from which absorption takes place. When the photon is reabsorbed by Eu^{2+}, the newly excited Eu^{2+} ion can re-emit the photon after some time delay, but there is also a small probability of nonradiative decay. The process of emission and reabsorption can occur any number of times, lengthening the decay time and lowering the light yield. Specifically problematic is that the probability of reabsorption scales with the distance a photon travels through the crystal and therefore depends on where in the crystal the scintillation event takes place. Because of this, the scintillation properties of SrI_2:Eu^{2+} typically worsen with increasing crystal size and Eu^{2+} concentration [8,15].

SrI_2 and EuI_2 are isostructural [16]. Because of this, it is possible to achieve any Eu^{2+} concentration in SrI_2 between 0% and 100%.

---

* Corresponding author.
E-mail address: c.vanaarle@tudelft.nl (C. van Aarle).

https://doi.org/10.1016/j.optmat.2024.116583
Received 19 September 2024; Accepted 15 December 2024

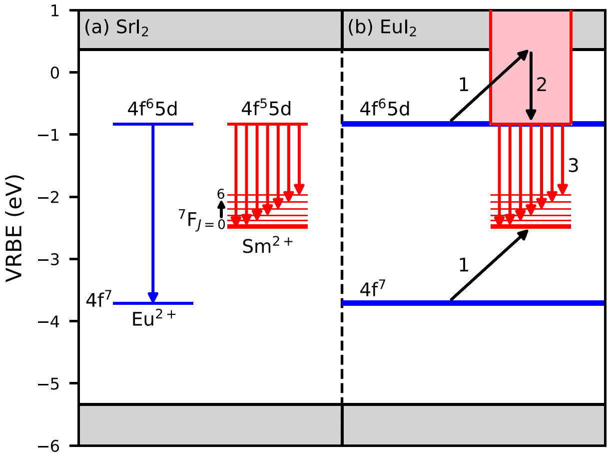

Fig. 1. (a) Vacuum referred binding energy diagram showing energy levels of Eu^{2+} and Sm^{2+} in the band gap of SrI_2. The diagram is constructed using the parameters published in [14]. (b) VRBE diagram illustrating the band structure of EuI_2:Sm^{2+}. When an excitation arrives on Sm^{2+}, thermal relaxation makes transfer back to Eu^{2+} impossible.

However, above a certain concentration, self-absorption is not the only phenomenon degrading the scintillation properties. At some point, the light yield will also start to decrease due to concentration quenching. This can be seen from the shortened decay time of 355 ns in EuI_2 [17] compared to the intrinsic decay time of approximately 700 ns of SrI_2:Eu^{2+} [13]. The two main problems for large SrI_2 crystals with high Eu^{2+} are therefore self-absorption and concentration quenching.

Another very bright Eu^{2+}-doped scintillator is CaI_2. Both undoped CaI_2 and with Eu^{2+}-doping have light yields reported in excess of 80,000 ph/MeV [18–20]. As CaI_2 has a different crystal structure than EuI_2, there is a limit to the dopant concentration. Another potential dopant would be Yb^{2+}, which is also sometimes researched as activator for scintillator applications [21–23]. YbI_2 does have the same crystal structure as CaI_2 and any concentration of Yb^{2+}-doping would be possible [24]. However, this is not interesting for scintillator applications, because the Yb^{2+} $4f^{13}5d$ → $4f^{14}$ emission contains a spin-forbidden component with ms decay time. The intensity of this component also increases with increasing Yb^{2+} concentration [25–27].

Sm^{2+}, on the other hand, does not have a slow spin-forbidden component, because its 4f subshell of Sm^{2+} is less than half filled in the ground state. Its energy levels in the band gap of SrI_2 are also displayed in Fig. 1a. In SrI_2, Sm^{2+} shows broad band $4f^55d \rightarrow 4f^6$ emission which can efficiently be detected with silicon based photodetectors. One large benefit of Sm^{2+} is that its emission is not as susceptible to self-absorption as the emission of Eu^{2+}. This is because the $4f^55d \rightarrow 4f^6$ transitions of Sm^{2+} can have any of the seven $4f^6[^7F_J]$ states as final state. Since absorption only takes place from the $4f^6[^7F_0]$ ground state, photons originating from the $4f^55d \rightarrow 4f^6[^7F_{1-6}]$ transitions will have a low probability of being reabsorbed.

The $4f^6 \rightarrow 4f^55d$ excitation bands of Sm^{2+} have high oscillator strength and span the entire visible spectrum, making it easily sensitised by for example Eu^{2+} and Yb^{2+}. By co-doping Eu^{2+} and Sm^{2+} in $CsBa_2I_5$, an energy resolution of 3.2% was attained [6]. When using Yb^{2+} as sensitiser in low (a few %) concentrations, a slow component in the Sm^{2+} emission was observed [25]. This slow component was caused by radiationless energy transfer of which the rate was limited by the spin-forbidden Yb^{2+} $4f^{13}5d \rightarrow 4f^{14}$ transition. One way to solve this slow energy transfer is to drastically increase the Yb^{2+} concentration, e.g., doping Sm^{2+} in compounds where Yb^{2+} is one of the host cations. Examples of this are $CsYbBr_3$:Sm^{2+}, $CsYbI_3$:Sm^{2+} and $YbCl_2$:Sm^{2+}. Sm^{2+} can efficiently emit in such compounds and shows near-infrared luminescence with a quenching temperature above 700 K [28]. It was also shown that Sm^{2+} shows luminescence in compounds with Eu^{2+} as host cation [29,30].

Fig. 1b illustrates the transfer from Eu^{2+} to Sm^{2+} in compounds with an Eu^{2+} host cation. Here, EuI_2 is chosen as an example. Because SrI_2 and EuI_2 are isostructural and the ionic radii of Sr^{2+} and Eu^{2+} differ by less than 1% [31], it is assumed that all energy levels lie at the same VRBE in both compounds. The Eu^{2+} $4f^7$ ground state is indicated as a narrow band of occupied states around −3.7 eV. Similarly, the lowest $4f^65d$ excited state is indicated with a narrow band of unoccupied states around −0.8 eV. The higher lying $4f^65d$ are not drawn for Eu^{2+}. The transition between the $4f^7$ ground state and lowest $4f^65d$ excited state forms the optical band gap of EuI_2. The conduction band minimum still lies at higher energy than the $4f^65d$ excited state, as it corresponds to an electron no longer bound to the hole in the 4f subshell of Eu^{2+}. An excitation of Eu^{2+} into the $4f^65d$ state can show ordinary Eu^{2+} $4f^65d \rightarrow 4f^7$ emission [17,32]. However, since it is surrounded by Eu^{2+} ions in the ground state and the Stokes shift is relatively small, it will likely hop over many Eu^{2+} sites before this emission occurs.

When doping EuI_2 with Sm^{2+}, the hopping of Eu^{2+} excitations eventually causes the excitation to end up on Sm^{2+}. This is indicated by Arrows 1 in Fig. 1b. The energy difference between the lowest $4f^{n-1}5d$ excited state of Sm^{2+} and its ground state is however much smaller for Sm^{2+} than for Eu^{2+}. Because of this, thermal relaxation to the lowest $4f^55d$ will take place as shown by Arrow 2. From here, not enough energy is available for the excitation to transfer back to Eu^{2+}, trapping it in place and allowing for efficient NIR emission (Arrow 3). Doping EuI_2 with Sm^{2+} therefore solves its problem of concentration quenching, and it also tackles the problem of self-absorption as the probability of Sm^{2+} to reabsorb its own emission is inherently low. When self-absorption and concentration quenching are absent, a similar light yield in excess of 80,000 ph/MeV could be expected for EuI_2:Sm^{2+}, as long as energy transfer from Eu^{2+} to Sm^{2+} is efficient. Analogous to this description, it is also expected that YbI_2:Sm^{2+} shows efficient NIR emission.

SrI_2:Sm^{2+} has already been studied both spectroscopically [33,34] and for NIR emitting scintillator applications [5]. The Sm^{2+} emission band has a maximum at 755 nm and has a decay time of 1.5 μs. This is among the fastest decay time reported for Sm^{2+} emission, as the decay time in most other compounds is at least 2 μs or longer [35]. As far as the authors are aware, there is no available literature on neither YbI_2:Sm^{2+} nor CaI_2:Sm^{2+}.

In this work, the scintillation characteristics of SrI_2:1%Sm^2, EuI_2:4%Sm^{2+} and YbI_2:1%Sm^{2+} single crystals grown by the vertical Bridgman method are assessed. The emission spectra and decay time under X-ray excitation are measured and an estimate of their light yield is made. Furthermore, more evidence is gathered that the self-absorption probability of the Sm^{2+} emission is low. This is done by determining which of the Sm^{2+} $4f^55d \rightarrow 4f^6[^7F_J]$ transitions are the most intense using optical spectroscopy. Lastly, the intrinsic luminescence decay times of the Sm^{2+} emission are measured and compared between the samples.

2. Experimental techniques

SrI_2:1%Sm^{2+}, EuI_2:4%Sm^{2+}, and YbI_2:1%Sm^{2+} single crystals were grown from molten mixtures of the respective binary iodides in sealed Ta ampoules by the vertical Bridgman technique. The reported Sm^{2+} doping was the nominal SmI_2 content of the melt. The purely divalent oxidation state of Sm was assured by adding a piece of 20 mg Sm metal to each batch of 2 g total weight. SrI_2 was synthesised from $SrCO_3$ (4N4, Alfa) and 57% HI acid (p.a. Merck), dried at 200 °C in vacuum, and purified by Bridgman crystal growth. EuI_2 and YbI_2 were prepared from the elements in a silica ampoule sealed under vacuum. Eu (3N, Metall Rare Earth Ltd.) or Yb (4N, Metall Rare Earth Ltd.) and I_2 (Merck, p. a., sublimed) were slowly heated to 650 °C. One end of the ampoule protruded from the tube furnace to avoid high iodine pressure during the reaction. After the reaction was finished, the ampoule was opened and heated in vacuum to remove excess I_2. The product was sealed in a silica ampoule and purified by Bridgman crystal growth. SmI_2 was prepared from SmI_3 by reduction with Sm (3N, Metall Rare Earth Ltd.) in a Ta ampoule sealed by He arc welding. SmI_3 was synthesised from the elements, as described above, and purified by sublimation under vacuum in a sealed silica ampoule. All materials are highly hygroscopic and Sm^{2+} compounds sensitive to oxidation. The syntheses and spectroscopic investigations were done under strictly dry and oxygen-free conditions in a glove box (H_2O and O_2 < 0.1 ppm) or sealed sample containers.

X-ray excited emission spectra were recorded using a Varex VF-80JM X-ray tube with tungsten anode as excitation source. The X-ray tube was operated at a voltage of 79 kV and a current of 1 mA. A 1 mm thick copper filter was used to block out the low energy X-rays to prevent radiation damage to the sample. The samples, which were sealed in a silica ampoule, were positioned in a sample chamber which was kept at a vacuum below 10^{-4} mbar during measurement. The light coming from the sample under a 90° angle with respect to the X-ray tube was focussed by a parabolic mirror into an optical fibre and read out using an Ocean Insight QEPro spectrometer.

X-ray excited decay curves were measured using a time correlated single photon counting technique. A Hamamatsu N5084-40 pulsed light excited X-ray tube with tungsten anode operated at 40 kV was used as excitation source. The X-ray tube was excited by a PicoQuant LDH-P-C-400M laser diode, and a start signal was generated upon triggering the laser diode. A bare crystal was mounted on the cold finger of a Janis N_2 cryostat and placed in a sample chamber with beryllium entrance window on the side of the X-ray tube. This action was performed inside a N_2 filled glovebox. During measurement, the sample chamber was kept at a vacuum below 10^{-4} mbar. Photons coming from the sample under a 90° angle with respect to the X-ray tube were detected using an ID Quantique ID100-50 single photon avalanche diode, generating a stop signal. The start and stop signal were fed into an Ortec 567 time-to-amplitude converter and read out using an Ortec AD114 16K analog-to-digital converter.

Pulse height spectra were recorded using an Advanced Photonix APD (type 630-70-72-510) operated at a bias voltage of 1570 V. Two Peltier coolers were used to stabilise the temperature of the APD at 260 K. The APD signal was converted using a Cremat CR-112 pre-amplifier and Ortec 672 spectroscopic amplifier. The resulting signal was read out using an Ortec 926 analog-to-digital converter. The bare and unpolished samples were mounted above the APD using the pressed powder method described in [36], in which the sample is surrounded by PTFE powder reflecting all scintillation photons towards the detector.

The absolute light yield of SrI_2:1%Sm^{2+} has been determined through the pulse height spectrum on a single crystal measured on the APD. The number of detected photons during an event that falls within the 662 keV photopeak was compared to the pulse height of ^{241}Am 17.8 keV directly absorbed in the APD. SrI_2:1%Sm^{2+} was used as a reference sample for determining the light yield of EuI_2:4%Sm^{2+} and YbI_2:1%Sm^{2+} using the set-up described for recording X-ray excited emission spectra. For this, single crystals of each compound were ground to a powder using a mortar and pestle. Identical sample holders with fused silica windows were filled in a glovebox with the powderised samples.

Photoluminescence emission spectra were recorded using a 450 W Xenon lamp and Horiba Gemini 180 monochromator as excitation source. The sample inside a silica ampoule was mounted on the cold finger of a Janis He cryostat. The sample chamber was kept at a vacuum below 10^{-4} mbar during measurement. The emission light coming from the sample under a 90° angle with respect to the excitation source was coupled into an optical fibre and read out using an Ocean Insight QEPro spectrometer. The excitation light was filtered out using an optical long pass filter placed between the sample and the optical fibre.

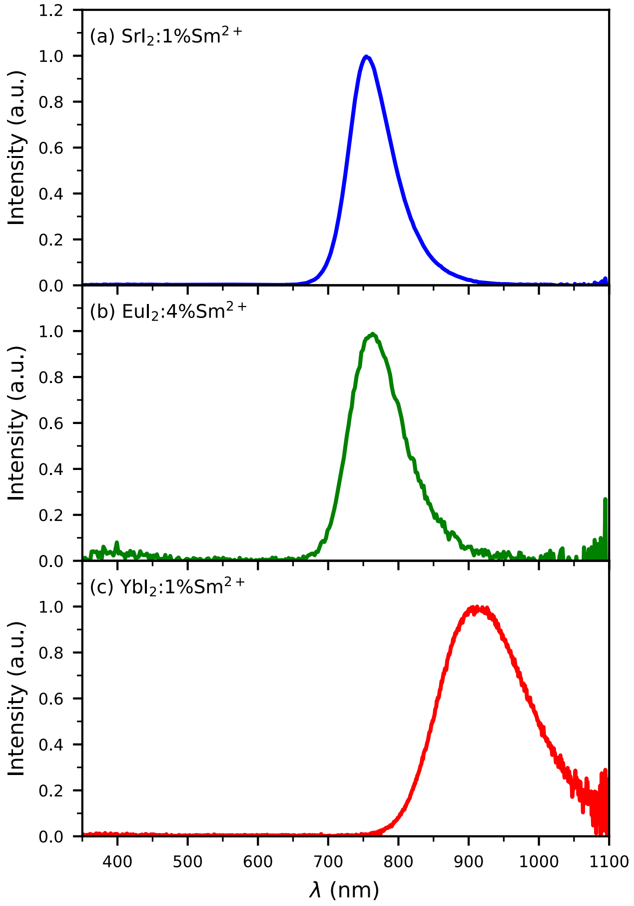

Fig. 2. X-ray excited emission spectra at room temperature of (a) SrI_2:1%Sm^{2+}, (b) EuI_2:4%Sm^{2+}, and (c) YbI_2:1%Sm^{2+}.

Photoluminescence excitation spectra were recorded using the excitation source, cryostat and sample chamber as for the photoluminescence emission spectra. The emission coming from the sample first passed through an optical long pass filter and a SpectraPro-SP2358 monochromator before being detected using a Hamamatsu R7600U-20 or H10330A-75 PMT. The spectra were corrected for the Xenon lamp spectrum and excitation monochromator by measuring the light intensity coming out of the monochromator using an Opto Diode UVG100 photodiode.

Photoluminescence decay curves were measured using an EKSPLA NT230 OPO laser as excitation source. The pulse width of the laser is 6 ns and it was operated with a repetition rate of 100 Hz. The sample inside a silica ampoule was mounted on the cold finger of a Janis N_2 cryostat. The emission coming from the sample passed through an optical long pass filter and SpectraPro-SP2358 monochromator before being detected using a Hamamatsu R7600U-20 or H10330A-75 PMT. The signal coming from the PMT was recorded using a CAEN DT5730 digitizer. The signals of multiple pulses were added up using the trigger signal from the laser driver for synchronisation.

3. Results

To assess whether the emission wavelength of the studied samples is suitable for read out with silicon based photodetectors, their room temperature X-ray excited emission spectra are shown in Fig. 2. It was previously assessed that the SrI_2:1%Sm^{2+} emission wavelength is close to the optimal emission wavelength for Sm^{2+}-doped scintillators [35]. Its emission spectrum in Fig. 2a shows a single emission band with

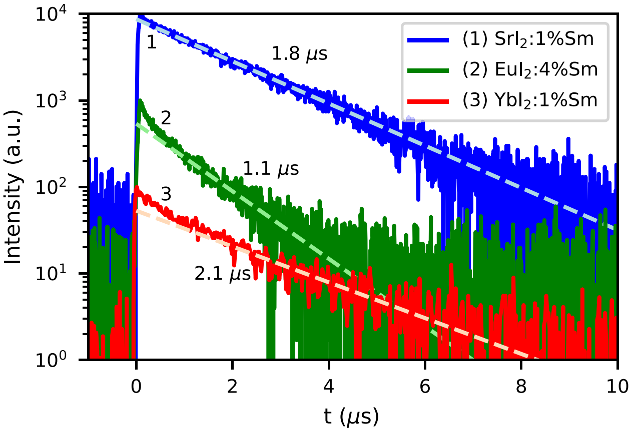

Fig. 3. X-ray excited decay curves at room temperature of (1) SrI_2:1%Sm^{2+}, (2) EuI_2:4%Sm^{2+}, and (3) YbI_2:1%Sm^{2+}. The fast components of EuI_2:4%Sm^{2+} and YbI_2:1%Sm^{2+} are ascribed to left over Eu^{2+} and Yb^{2+} emission, respectively.

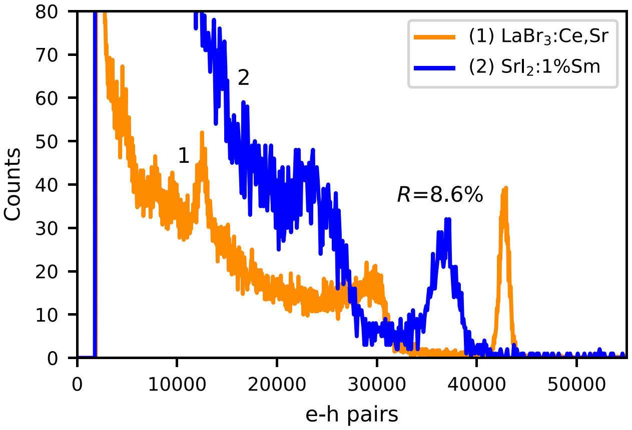

Fig. 4. Pulse height spectra of (1) $LaBr_3$:Ce^{3+},Sr^{2+} and (2) SrI_2:1%Sm^{2+} measured on an APD. The light yield of SrI_2:1%Sm^{2+} is estimated to be 57,000 ph/MeV.

maximum at 755 nm, in accordance with literature values [5,33,34]. This band is assigned to the Sm^{2+} $4f^55d \rightarrow 4f^6$ emission.

The X-ray excited emission spectrum of EuI_2:4%Sm^{2+} in Fig. 2b looks almost identical to that of SrI_2:1%Sm^{2+}. This is according to expectation, since both SrI_2 and EuI_2 have the same crystal structure and the similar ionic radii of Sr^{2+} and Eu^{2+} [31]. Because of this, the chemical environment of Sm^{2+} is almost identical in both compounds, resulting in the same wavelength and shape of the emission band. This means that the emission spectrum of EuI_2:4%Sm^{2+} is also close to optimal for read out with silicon based photodetectors.

The X-ray excited emission spectrum of YbI_2:1%Sm^{2+} is shown in Fig. 2c. Like SrI_2:1%Sm^{2+} and EuI_2:4%Sm^{2+}, it shows a single emission band in the near-infrared. In YbI_2:1%Sm^{2+} this emission band is however shifted to longer wavelengths and has a maximum at 910 nm. As YbI_2 and CaI_2 have the same crystal structure [24] and the ionic radii of Yb^{2+} and Ca^{2+} are almost identical [31], the Sm^{2+} $4f^55d \rightarrow 4f^6$ emission is expected to lie at the same wavelength in both compounds, similar as is the case for SrI_2 and EuI_2. Because of this, a prediction of the Sm^{2+} emission wavelength in YbI_2 can be made based on the Eu^{2+} emission wavelength in CaI_2. The Sm^{2+} $4f^55d \rightarrow 4f^6[^7F_0]$ transition always lies at approximately 1.22 eV lower energy than the Eu^{2+} $4f^65d \rightarrow 4f^7$ transition in the same compound [37]. The Eu^{2+} emission wavelength lies at 470 nm in CaI_2 [18,38], from which follows that the Sm^{2+} emission wavelength in YbI_2 is expected around 890 nm. Based on this, the strong emission band at 910 nm is also ascribed to the Sm^{2+} $4f^55d \rightarrow 4f^6$ transition. The longer emission wavelength compared to SrI_2:1%Sm^{2+} and EuI_2:4%Sm^{2+} is expected due to the increased crystal field splitting, which is caused by the 6-fold coordination of Sm^{2+} in YbI_2. Because almost all of the emission lies at wavelengths longer than 800 nm, it can no longer be detected by silicon based photodetectors with near 100% efficiency.

Table 1
Overview of the scintillation properties of SrI_2:1%Sm^{2+}, EuI_2:4%Sm^{2+}, and YbI_2:1%Sm^{2+}.

Compound	λ (nm)	τ (μs)	Light yield (ph/MeV)
SrI_2:1%Sm^{2+}	755	1.8	57,000
EuI_2:4%Sm^{2+}	755	1.1	5,300
YbI_2:1%Sm^{2+}	910	2.1	6,800

To confirm that excitations arrive at Sm^{2+} quickly after excitation, the room temperature X-ray excited decay curves are shown in Fig. 3. The decay curve of SrI_2:1%Sm^{2+} (Curve 1) is well approximated by a single exponential decay curve with decay time of 1.8 μs, which is 300 ns longer than 1.5 μs reported in literature [5,33,34].

Unlike SrI_2:Sm^{2+}, the decay curve of EuI_2:4%Sm^{2+} (Curve 2) does not follow a single exponential function, but has a fast component. This fast component is attributed to Eu^{2+} emission, as the on average around 10 keV X-rays excite the sample primarily at the surface that the detector is pointing at. This is different to the X-ray excited emission measurements in Fig. 2b, where the higher energy X-rays primarily excite the bulk of the sample. The main component in the EuI_2:4%Sm^{2+} decay curve is attributed to the Sm^{2+} emission and has a decay time of 1.1 μs. This is shorter than the decay time of SrI_2:1%Sm^{2+}, which as far as the authors are aware is the shortest reported radiative decay time for Sm^{2+} emission. No slower components than 1.1 μs are detected, which indicates that the decay time of EuI_2:4%Sm^{2+} is not limited by the rate of energy transfer from Eu^{2+} to Sm^{2+}.

The decay curve of YbI_2:1%Sm^{2+} also has a fast component, which is attributed to Yb^{2+} emission for the same reasoning as for EuI_2:4%Sm^{2+}. The main component has a decay time of 2.1 μs, which is slower than SrI_2:1%Sm^{2+} and EuI_2:4%Sm^{2+}. The longer decay time compared to EuI_2:4%Sm^{2+} is in line with the expected λ^3 dependence. However, as the expected decay time for Sm^{2+} emission around 900 nm is expected to be between 3 μs and 4 μs [35], the 2.1 μs of YbI_2:1%Sm^{2+} is still fast for its emission wavelength. Again, no slower components than 2.1 μs are detected, indicating that also the spin-forbidden transitions of Yb^{2+} do not cause slow energy transfer to Sm^{2+}.

The pulse height spectrum of SrI_2:1%Sm^{2+} is shown in Fig. 4. For comparison, it also shows the pulse height spectrum of $LaBr_3$:Ce^{3+},Sr^{2+} which has a light yield of 78,000 ph/MeV [39]. For SrI_2:1%Sm^{2+}, over 37,000 photons were detected for events that fall within the 662 keV photopeak. Assuming near 100% photon detection efficiency of the set-up, the light yield is determined to be around 57,000 ph/MeV. The energy resolution attained with this crystal is 8.6%.

An attempt to measure a pulse height spectrum using the other samples was not successful. Therefore, their light yield was determined from the intensity of their X-ray excited emission spectrum using SrI_2:1%Sm^{2+} as reference. The light yield of the EuI_2:4%Sm^{2+} and YbI_2:1%Sm^{2+} is 5,300 ph/MeV and 6,800 ph/MeV, respectively. This is about 10 times lower than that of SrI_2:1%Sm^{2+}. The scintillation characteristics of all samples are summarised in Table 1.

To confirm that excitations of Eu^{2+} and Yb^{2+} arrive at Sm^{2+}, the photoluminescence excitation and emission spectra at 10 K are shown in Fig. 5. The emission spectrum of SrI_2:1%Sm^{2+} excited at 350 nm is shown in Fig. 5a. This excitation wavelength corresponds to one of the higher energy Sm^{2+} $4f^6 \rightarrow 4f^55d$ transitions. The emission spectrum contains only the Sm^{2+} emission around 755 nm. At 10 K, the Sm^{2+} $4f^55d \rightarrow 4f^6$ emission consists of multiple emission bands. The shape of the emission spectrum is in accordance with data from Karbowiak et al. [34]. Each of these bands corresponds to a different $4f^6[^7F_J]$ state

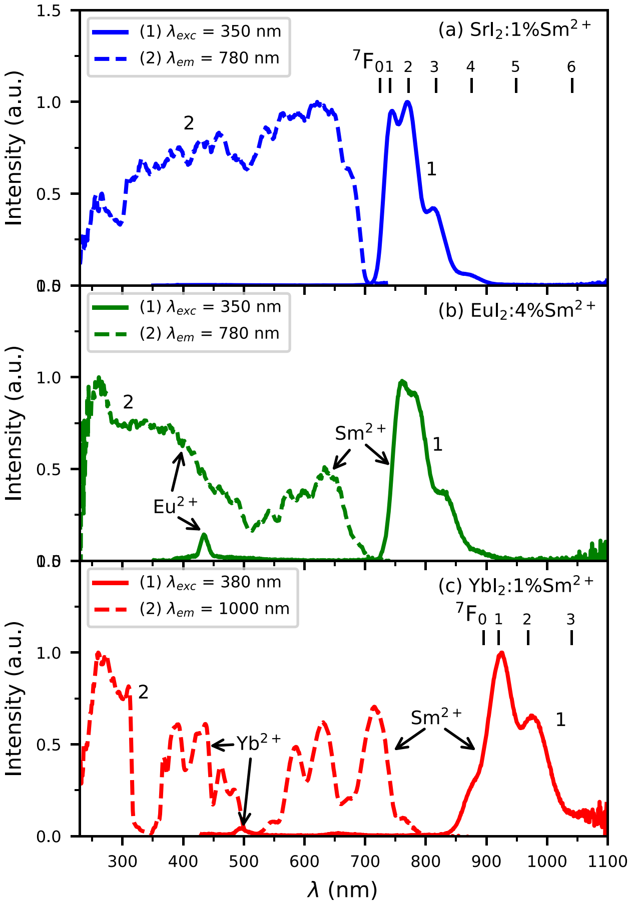

Fig. 5. Photoluminescence excitation and emission spectra at 10 K of (a) SrI_2:1%Sm^{2+}, (b) EuI_2:4%Sm^{2+}, and (c) YbI_2:1%Sm^{2+}. Most of the Sm^{2+} emission comes from the $4f^55d \rightarrow 4f^6[^7F_{1-2}$ transitions.

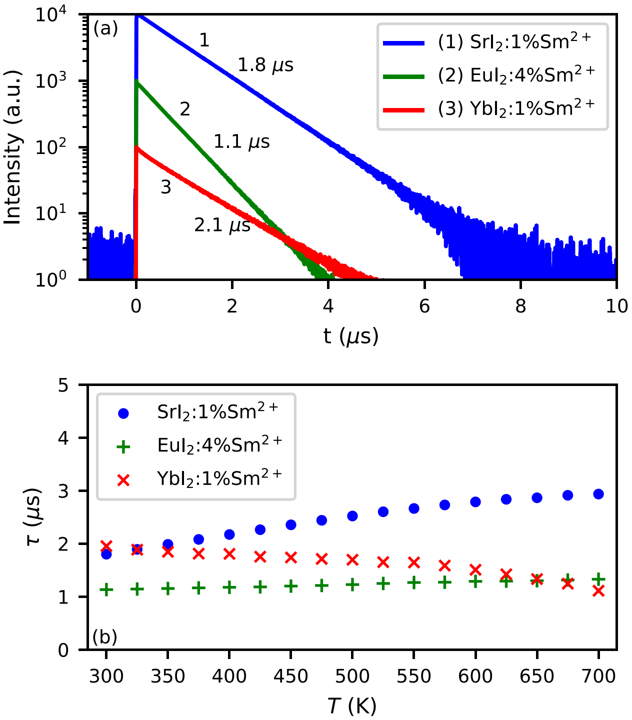

Fig. 6. (a) Photoluminescence decay curves of the Sm^{2+} $4f^55d \rightarrow 4f^6$ emission at 300 K in (1) SrI_2:1%Sm^{2+}, (2) EuI_2:4%Sm^{2+}, and (3) YbI_2:1%Sm^{2+}. (b) The photoluminescence decay time of the Sm^{2+} $4f^55d \rightarrow 4f^6$ emission versus temperature.

as final state. The expected maxima of each of these emission bands is calculated from the Eu^{2+} emission wavelength in SrI_2:Eu^{2+} [8,13,37] and indicated by the black vertical lines. This shows that the Sm^{2+} emission primarily comes from the $4f^55d \rightarrow 4f^6[^7F_{1-4}]$ transitions, and most importantly not from the $4f^55d \rightarrow 4f^6[^7F_0]$ transition. This significantly reduces the self-absorption probability in SrI_2:Sm^{2+} compared to SrI_2:Eu^{2+} [5,35,40]. The excitation spectrum monitoring the Sm^{2+} emission at 780 nm (Curve 2) contains all the overlapping $4f^6 \rightarrow 4f^55d$ bands and is in good accordance with literature [33].

Fig. 5b shows the 10 K photoluminescence emission and excitation spectra of EuI_2:4%Sm^{2+}. Similar to the emission spectrum of SrI_2:1%Sm^{2+}, the emission spectrum of EuI_2:4%Sm^{2+} excited at 350 nm also contains the Sm^{2+} emission around 755 nm. The shape of the emission spectrum is almost identical to that of SrI_2:1%Sm^{2+}. It contains the same $4f^55d \rightarrow 4f^6[^7F_J]$ emission bands which also have almost the same relative intensities. In addition, it contains a low intensity band around 430 nm which is ascribed to the Eu^{2+} $4f^65d \rightarrow 4f^7$ emission [17,32]. As the sample was excited with 350 nm light, the high Eu^{2+} concentration causes most of the light to be absorbed near the sample surface and as a result some Eu^{2+} emission can be detected, similar to what was observed in Fig. 3b.

The excitation spectrum monitoring the Sm^{2+} emission of EuI_2:4%Sm^{2+} at 780 nm (Curve 2) has many similarities with that of SrI_2:1%Sm^{2+} between 430 nm and 700 nm. This is where the excitation spectrum exclusively consists out of Sm^{2+} $4f^6 \rightarrow 4f^55d$ bands. Similar to how the emission spectra between the two samples closely resemble each other, the excitation bands of Sm^{2+} do as well. At wavelengths shorter than 430 nm, Eu^{2+} also starts to absorb while Sr^{2+} is not optically active. Therefore, at wavelengths shorter than 430 nm, the excitation spectra between SrI_2:1%Sm^{2+} and EuI_2:4%Sm^{2+} differ in shape. The presence of these Eu^{2+} $4f^7 \rightarrow 4f^65d$ absorption bands in the excitation spectrum of the Sm^{2+} indicates that Eu^{2+} excitations are transferred to Sm^{2+}.

The 10 K photoluminescence emission and excitation spectra of YbI_2:1%Sm^{2+} are shown in Fig. 5c. Similar to EuI_2:4% Sm^{2+}, the emission spectrum (Curve 1) contains a weak emission band around 500 nm that can be ascribed to the Yb^{2+} $4f^{13}5d \rightarrow 4f^{14}$ emission. The Sm^{2+} emission between 850 nm and 1100 nm again consists out of multiple bands. Just like in Fig. 5a, the expected wavelengths of the $4f^55d \rightarrow 4f^6[^7F_J]$ transitions are marked with black vertical lines, which line up well with the different emission bands in the spectrum. Again, the transition to the $4f^6[^7F_0]$ ground state is relatively weak, which reduces the probability of self-absorption. Just like for EuI_2:Sm^{2+}, the excitation spectrum monitoring the Sm^{2+} emission at 1000 nm (Curve 2) consists of Sm^{2+} bands between 450 nm and 800 nm. At wavelengths shorter than 450 nm, the Yb^{2+} bands are dominant in the excitation spectrum.

Fig. 6a shows the room temperature photoluminescence decay curves of the Sm^{2+} emission in all three samples upon exciting one of the Sm^{2+} $4f^6 \rightarrow 4f^55d$ transitions. All three samples show single exponential decay. SrI_2:1%Sm^{2+} has a decay time 1.8 μs, EuI_2:4%Sm^{2+} has a decay time of 1.1 μs, and YbI_2:1%Sm^{2+} has a decay time of 2.1 μs. All these decay times correspond to the slowest components observed under X-ray excitation (Fig. 3), confirming that these components belong to the Sm^{2+} emission.

To show that the Sm^{2+} is not quenched at room temperature, the decay time of the Sm^{2+} emission as a function of temperature is shown in Fig. 6b. SrI_2:1%Sm^{2+} shows a gradual lengthening of the decay time with temperature. For Eu^{2+} emission this is often a sign of self-absorption. However, for Sm^{2+}, this is intrinsic behaviour and can be ascribed to thermal excitation from the $4f^55d$ state to the higher lying $4f^6[^5D_0]$ state [35]. This occurs, because the energy gap between the two states is only about 5 meV and can be easily crossed at room temperature. No signs of thermal quenching are observed, even at a temperature of 700 K.

EuI_2 also shows some lengthening of the decay time with increasing temperature. This is expected due to similar emission wavelength between EuI_2:4%Sm^{2+} and SrI_2:1%Sm^{2+}, meaning the energy gap between the $4f^55d$ state and $4f^6[^5D_0]$ state is also about 5 meV. The effect is much smaller than in SrI_2:1%Sm^{2+}. Also, no thermal quenching can be observed up to 700 K.

In YbI_2:1%Sm^{2+}, the energy gap between the Sm^{2+} $4f^55d$ state and the $4f^6[^5D_0]$ state is about 280 meV. With an energy gap of this size, the thermal equilibrium hardly changes between 300 K and 700 K. The decay time therefore does not lengthen with increasing temperature, but instead the decay becomes slightly faster. Above 600 K, the onset of thermal quenching is visible for YbI_2:1%Sm^{2+}.

4. Discussion

Sm^{2+} as an activator allows the use of host compounds that contain Eu^{2+} and Yb^{2+} as cations, which can often fully replace Sr^{2+} and Ca^{2+} in the same crystal structure. It was shown in Fig. 5 that spectroscopically, SrI_2:1%Sm^{2+} and EuI_2:4%Sm^{2+} show great similarity. The excitation bands belonging to the Sm^{2+} are almost identical between the compounds, and so are the structures in their emission spectra. Especially the similarity in emission spectra is important for application, as the emission spectrum of SrI_2:1%Sm^{2+} lies close to optimal for Sm^{2+}-doped scintillators. It lies almost entirely at a wavelength shorter than 800 nm, where some silicon based photodetectors can be exploited to gain a photodetection efficiency close to 100% [36]. However, its wavelength is still long enough that the $4f^55d$ level lies just below the $4f^6[^5D_0]$ level, avoiding lengthening of the decay time [35]. Additionally, most of the emission arises from the Sm^{2+} $4f^55d \rightarrow 4f^6[^7F_{1-2}]$ transitions. The near absence of the $4f^55d \rightarrow 4f^6[^7F_0]$ emission makes the probability of self-absorption small, a problem that prevents the use of large crystals in its Eu^{2+}-doped counterpart [8]. Just like SrI_2:1%Sm^{2+}, the emission spectrum of EuI_2:4%Sm^{2+} also has all these beneficial characteristics.

Opposed to SrI_2:1%Sm^{2+} and EuI_2:4%Sm^{2+}, the emission spectrum of YbI_2:1%Sm^{2+} lies almost entirely at wavelengths longer than 800 nm and spans all the way to 1100 nm. While this wavelength can still be detected with silicon based photodetectors, some unrecoverale losses will likely occur due to the transmission of scintillation photons through the detector [36]. It is therefore considered less suitable for application as a NIR scintillator.

The longer emission wavelength of YbI_2:1%Sm^{2+} compared to SrI_2:1%Sm^{2+} and EuI_2:4%Sm^{2+} is ascribed to its different crystal structure. As Sm^{2+} is 6-fold coordinated in YbI_2 and 7-fold coordinated in SrI_2 and EuI_2, the larger crystal field splitting causes a lower energy of the $4f^55d$ level. In iodides, the crystal field splitting of the $4f^{n-1}5d$ levels can be 0.5 eV larger on octahedral (6-fold coordinated) and cubic (8-fold coordinated) sites compared to sites where the crystal field splitting is small, such as the case for 7-fold and 9-fold coordination [41]. Table 2 shows an overview of the Sm^{2+} emission wavelength and coordination number in different iodide compounds. All compounds in which Sm^{2+} is 6-fold or 8-fold coordinated have an emission wavelength of 800 nm or longer. On the other hand, all compounds in which Sm^{2+} has a coordination number of 7 emit in the ideal wavelength range between 730 nm and 800 nm. As a rule of thumb, the search for ideal host materials should therefore be primarily focussed on iodides with 7-fold coordination. Also the 9-fold coordinated BaI_2 emits in the desired wavelength range and would be a good candidate. It is possible to expand the search from iodides to lighter halides, as the smaller nephelauxetic effect would move the $4f^{n-1}5d$ centroid to higher energies [42]. However, this would come at the expense of an increase of the band gap [43].

Table 2
Comparison of the Sm^{2+} $4f^55d \rightarrow 4f^6$ emission wavelength and the coordination number of Sm^{2+} in several compounds. *Estimate of the Sm^{2+} $4f^55d \rightarrow 4f^6[^7F_0]$ emission wavelength based on the Eu^{2+} $4f^65d \rightarrow 4f^7$ emission.

Compound	λ (nm)	CN	Reference
$CsSrI_3$	841	6	[44]
$CsYbI_3$	800	6	[28]
Cs_4EuI_6	848	6	[29]
NaI	850	6	[45]
YbI_2	910	6	This work
CaI_2	890*	6	[18,38]
SrI_2	755	7	[5,33,34]
EuI_2	755	7	This work
$CsBa_2I_5$	755	7	[6]
KBa_2I_5	791*	7	[46]
K_2BaI_4	801*	8	[46]
BaI_2	730*	9	[47,48]

One of the downsides of using Sm^{2+} as an activator is its relatively long decay time compared to other activators such as Eu^{2+} and Ce^{3+}. Sm^{2+} emission will always be much slower than the fast decay of Ce^{3+}, which is for example 16 ns in $LaBr_3$ [49]. However, Eu^{2+} typically shows an intrinsic decay time between 0.5 μs and 1 μs [13,50–53]. The decay time of Eu^{2+}-doped scintillators can however be significantly longer due to their inherent self-absorption problems. Decay times of well over 2 μs are reported for large SrI_2:Eu^{2+} crystals with a Eu^{2+} concentration below 5% [54–56]. This is where the decay time of Sm^{2+} becomes interesting, as similar lengthening in large crystals is not expected for Sm^{2+} emission due to its low probability of self-absorption.

As far as the authors are aware, SrI_2:Sm^{2+} shows the shortest reported radiative decay time of $4f^55d \rightarrow 4f^6$ emission with a value of 1.5 μs [5,33,34]. In this work, a value of 1.8 μs is reported. This is still faster than other Sm^{2+}-doped iodides, as no reports of decay times shorter than 2 μs could be found. Even a decay time of 1.8 μs makes it faster than the above mentioned scintillation decay of large SrI_2:Eu^{2+} crystals.

The decay time of EuI_2:4%Sm^{2+} is only 1.1 μs (Figs. 3 and 6). It was shown in Fig. 6 that this short decay time is not caused by thermal quenching, meaning that the radiative decay time of Sm^{2+} is significantly shorter in EuI_2 than in SrI_2. Spectroscopically, both compounds are very similar. The coordination of Sm^{2+} and emission wavelengths are almost identical, meaning these likely do not contribute significantly to the change in decay time. A logical contribution left is then the refractive index n, which is different between the compounds. The decay time rapidly shortens with an increase in refractive index, scaling approximately with n^5 [57]. Therefore, only a 5% difference refractive index between SrI_2 and EuI_2 would be enough to explain shortening of the Sm^{2+} decay time by several 100 ns.

When two compounds have similar crystal structure, lattice parameters and anion types, their difference in refractive index is primarily determined by the cation ionisation energy [58]. This is because the weakest bound electrons contribute most to the polarisability of the cations. While the binding energy of the Sr^{2+} core electrons lies well below the valence band maximum, the ionisation energy of Eu^{2+} is much smaller due to the many occupied $4f^7$ states being present in the band gap, as shown in the VRBE diagram in Fig. 1. This effect could be confirmed by comparing the refractive index of SrI_2 and EuI_2, however no data could be found for the refractive index of EuI_2. Luckily, a comparison between the refractive indices of the isostructural SrF_2 ($n = 1.44$ [59]) and EuF_2 ($n = 1.55$ [60]) also shows a significant increase in n upon replacing Sr^{2+} by Eu^{2+}. This increase is large enough to cause a change in luminescence decay time of the order of magnitude as observed between SrI_2 and EuI_2. The short decay time of 1.1 μs in EuI_2 is therefore ascribed to the higher refractive index compared to SrI_2. The same argument should hold when replacing Ca^{2+} with Yb^{2+}, as also the occupied $4f^{14}$ states of Yb^{2+} are present in the band gap.

Among NIR emitting scintillators, the light yield of 57,000 ph/MeV reported for SrI_2:1%Sm^{2+} in this work is comparable to the 60,000 ph/MeV reported for Cs_2HfI_6 [61,62]. It also surpasses previous attempts at Sm^{2+} (co-)doped SrI_2, which stopped at 42,000 ph/MeV. Compared to SrI_2:Eu^{2+}, for which light yields of over 80,000 ph/MeV are reported, the light yield is still low. However, the light yield of SrI_2:Eu^{2+} is maximal for Eu^{2+} concentrations between 5% and 10%. It is therefore expected that further improvements of SrI_2:Sm^{2+} are possible by optimising the Sm^{2+} concentration.

No fundamental reason could be found for the relatively poor light yield of EuI_2:4%Sm^{2+} and YbI_2:1%Sm^{2+}. The Sm^{2+} emission is not quenched under photoluminescence. Especially for EuI_2:4%Sm^{2+}, no signs of thermal quenching were visible even up to a temperature of 700 K. This indicates that excitations are already lost before they end up on Sm^{2+}. This suggests that the crystal quality is suboptimal and significant improvements can be made through optimisation of crystal growth and dopant concentration. This would be especially interesting for EuI_2:Sm^{2+}, as its emission wavelength and scintillation decay time of 1.1 μs are the most ideal of any Sm^{2+}-doped compound reported so far.

5. Conclusions

The scintillation properties of SrI_2:1%Sm^{2+}, EuI_2:4%Sm^{2+} and YbI_2:1%Sm^{2+} were assessed. SrI_2:1%Sm^{2+} and EuI_2:4%Sm^{2+} have almost identical emission spectra, which almost exclusively consist of the Sm^{2+} $4f^55d \rightarrow 4f^6$ emission. The similarities in emission spectrum are ascribed to both compounds having the same crystal structures in combination with Sr^{2+} and Eu^{2+} having almost identical ionic radius. Both compounds however show a difference in the decay time of the Sm^{2+} $4f^55d \rightarrow 4f^6$ emission, which is 1.8 μs in SrI_2:1%Sm^{2+} and shortens to 1.1 μs in EuI_2:4%Sm^{2+}. The Sm^{2+} emission decay time in EuI_2 is the fastest reported in literature so far. The Sm^{2+} $4f^55d \rightarrow 4f^6$ emission in YbI_2:1%Sm^{2+} has a maximum at 910 nm, which is at too long wavelength for efficient detection with silicon based photodetectors. With a decay time of 2.1 μs, it also has the longest scintillation decay of the samples in this work. Emission coming from the Sm^{2+} $4f^55d \rightarrow 4f^6[^7F_{1-2}]$ transitions is the strongest in all compounds reported in this work, while the emission band corresponding to the $4f^55d \rightarrow 4f^6[^7F_0]$ transition has low intensity. As a consequence, the probability of self-absorption in these Sm^{2+} is expected to be low, especially when compared to Eu^{2+}-doped compounds such as SrI_2:Eu^{2+}. Because of this, SrI_2:Sm^{2+} and EuI_2:Sm^{2+} are identified as interesting candidates for further optimisation to develop near-infrared emitting scintillators.

CRediT authorship contribution statement

Casper van Aarle: Conceptualization, Investigation, Visualization, Writing – original draft. **Daniel A. Biner:** Resources. **Karl W. Krämer:** Resources, Writing – review & editing. **Pieter Dorenbos:** Funding acquisition, Writing – review & editing.

Declaration of competing interest

The authors declare that they have no known competing financial interests or personal relationships that could have appeared to influence the work reported in this paper.

Acknowledgements

This research was subsidised by the TTW/OTP grant no. 18040 of the Dutch Research Council.

Data availability

Data will be made available on request.

References

[1] C.M. Combes, P. Dorenbos, C.W.E. van Eijk, K.W. Krämer, H.U. Güdel, J. Lumin. 82 (1999) 299.

[2] E.V.D. van Loef, P. Dorenbos, C.W.E. van Eijk, K. Krämer, H.U. Güdel, Appl. Phys. Lett. 77 (2000) 1467.

[3] E.V.D. van Loef, P. Dorenbos, C.W.E. van Eijk, K. Krämer, H.U. Güdel, Appl. Phys. Lett. 79 (2001) 1573.

[4] M.S. Alekhin, J.T.M. de Haas, I.V. Khodyuk, K.W. Krämer, P.R. Menge, V. Ouspenski, P. Dorenbos, Appl. Phys. Lett. 102 (2013) 151915.

[5] R.H.P. Awater, M.S. Alekhin, D.A. Biner, K.W. Krämer, P. Dorenbos, J. Lumin. 212 (2019) 1.

[6] Weronika Wolszczak, Karl W. Krämer, Pieter Dorenbos, Phys. Status Solidi R 13 (2019) 1900158.

[7] Takayuki Yanagida, Masanori Koshimizu, Go Okada, Takahiro Kojima, Junya Osada, Noriaki Kawaguchi, Opt. Mater. 61 (2016) 119.

[8] Mikhail S. Alekhin, Johan T.M. de Haas, Karl W. Krämer, Pieter Dorenbos, IEEE Trans. Nucl. Sci. 58 (2011) 2519.

[9] Nerine J. Cherepy, Giulia Hull, Alexander D. Drobshoff, Stephen A. Payne, Edgar van Loef, Cody M. Wilson, Kanai S. Shah, Utpal N. Roy, Arnold Burger, Lynn A. Boatner, Woon-Seng Choong, William W. Moses, Appl. Phys. Lett. 92 (2008) 083508.

[10] Leonard Alaribe, Christian Disch, Alex Fauler, Ralf Engels, Egbert Keller, Angelica Cecilia, Tomy dos Santos Rolo, Elias Hamann, Michael Fiederle, IEEE Trans. Nucl. Sci. 59 (2012) 2193.

[11] L.A. Boatner, J.O. Ramey, J.A. Kolopus, R. Hawrami, W.M. Higgins, E. van Loef, J. Glodo, K.S. Shah, Emmanuel Rowe, Pijush Bhattacharya, Eugene Tupitsyn, Michael Groza, Arnold Burger, N.J. Cherepy, S.A. Payne, J. Cryst. Growth 312 (2010) 1213.

[12] Yuntao Wu, Qi Li, Daniel J. Rutstrom, Ian Greeley, Luis Stand, Matthew Loyd, Merry Koschan, Charles L. Melcher, Nucl. Instrum. Methods A 954 (2020) 161242.

[13] Jarek Glodo, Edgar V. van Loef, Nerine J. Cherepy, Stephen A. Payne, Kanai S. Shah, IEEE Trans. Nucl. Sci. 57 (2010) 1228.

[14] Pieter Dorenbos, Aday Josef, Johan T.M. de Haas, Karl W. Krämer, J. Lumin. 208 (2019) 463.

[15] Taketoshi Kawai, Shiro Sakuragi, Satoshi Hashimoto, J. Lumin. 176 (2016) 58.

[16] H. Bärnighausen, N. Schultz, Acta Crystallogr. Sect. B 25 (1969) 1104.

[17] D.I. Galimov, R.G. Bulgakov, Luminescence 34 (2019) 127.

[18] R. Hofstadter, E.W. O'Dell, C.T. Schmidt, Rev. Sci. Instrum. 35 (1964) 246.

[19] Kei Kamada, Takashi Iida, Takaki Ohata, Masao Yoshino, Shoki Hayasaka, Yasuhiro Shoji, Shiro Sakuragi, Shunsuke Kurosawa, Yuui Yokota, Yuji Ohashi, Akira Yoshikawa, Ceram. Int. 43 (2017) S423.

[20] Takashi Iida, Kei Kamada, Masao Yoshino, Kyoung Jin Kim, Koichi Ichimura, Akira Yoshikawa, Nucl. Instrum. Methods A 958 (2020) 162629.

[21] Emmanuel Rowe, Pijush Bhattacharya, Eugene Tupitsyn, Michael Groza, Arnold Burger, Nerine J. Cherepy, Steve A. Payne, Benjamin W. Sturm, C. Pédrini, IEEE Trans. Nucl. Sci. 60 (2013) 1057.

[22] Mikhail S. Alekhin, Daniel A. Biner, Karl W. Krämer, Pieter Dorenbos, Opt. Mater. 37 (2014) 382.

[23] Kohei Mizoi, Yutaka Fujimoto, Daisuke Nakauchi, Masanori Koshimizu, Takayuki Yanagida, Keisuke Asai, J. Lumin. 240 (2021) 118399.

[24] Walter Döll, Wilhelm Klemm, Z. Anorg. Allg. Chem. 241 (1939) 239.

[25] Casper van Aarle, Karl W. Krämer, Pieter Dorenbos, J. Lumin. 238 (2021) 118257.

[26] Yuntao Wu, Bryan C. Chakoumakos, Hongliang Shi, Mao-Hua Du, Ian Greeley, Matthew Loyd, Daniel J. Rutstrom, Luis Stand, Merry Koschan, Charles L. Melcher, J. Lumin. 201 (2018) 460.

[27] Daniel Rutstrom, Luis Stand, Bogdan Dryzhakov, Merry Koschan, Charles L. Melcher, Mariya Zhuravleva, Opt. Mater. 110 (2020) 110536.

[28] Casper van Aarle, Karl W. Krämer, Pieter Dorenbos, J. Lumin. 251 (2022) 119209.

[29] Casper van Aarle, Karl W. Krämer, Pieter Dorenbos, J. Mater. Chem. C 11 (2023) 2336.

[30] Xuemin Wen, Petr Prusa, Linhart Vladimir, Tomas Parkman, Vojtech Vanecek, Dalibor Panek, Martin Nikl, Shuangliang Cheng, Qian Wang, Guohao Ren, Yuntao Wu, ACS Appl. Electron. Mater. 5 (2023) 3507.

[31] R.D. Shannon, Acta Crystallogr. A 32 (1976) 751.

[32] E. Rogers, P. Dorenbos, J.T.M. de Haas, E. van der Kolk, J. Phys. Condens. Mat. 24 (2012) 275502.

[33] Mikhail S. Alekhin, Roy H.P. Awater, Daniel A. Biner, Karl W. Krämer, Johan T.M. de Haas, Pieter Dorenbos, J. Lumin. 167 (2015) 347.

[34] Mirosław Karbowiak, Piotr Solarz, Radosław Lisiecki, Witold Ryba-Romanowski, J. Lumin. 195 (2018) 159.

[35] Casper van Aarle, Karl W. Krämer, Pieter Dorenbos, J. Lumin. 266 (2024) 120329.

[36] Johan T.M. de Haas, Pieter Dorenbos, IEEE Trans. Nucl. Sci. 55 (2008) 1086.

[37] P. Dorenbos, J. Phys. Condens. Mat. 15 (2003) 575.

[38] L.A. Boatner, J.O. Ramey, J.A. Kolopus, John S. Neal, Nucl. Instrum. Methods A 786 (2015) 23.

[39] Mikhail S. Alekhin, Daniel A. Biner, Karl W. Krämer, Pieter Dorenbos, J. Appl. Phys. 113 (2013) 224904.

[40] Pieter Dorenbos, Opt. Mater. X. 1 (2019) 100021.

[41] P. Dorenbos, J. Alloy. Compd. 341 (2002) 156.

[42] P. Dorenbos, J. Lumin. 104 (2003) 239.

[43] Pieter Dorenbos, Opt. Mater. 69 (2017) 8.

[44] W. Wolszczak, K.W. Krämer, P. Dorenbos, J. Lumin. 222 (2020) 117101.

[45] M. Guzzi, G. Baldini, J. Lumin. 6 (1973) 270.

[46] L. Stand, M. Zhuravleva, B. Chakoumakos, J. Johnson, A. Lindsey, C.L. Melcher, J. Lumin. 169 (2016) 301.

[47] J. Selling, M.D. Birowosuto, P. Dorenbos, S. Schweizer, Phys. Status Solidi C 4 (2007) 976.

[48] Zewu Yan, Gautam Gundiah, Gregory A. Bizarri, Eric C. Samulon, Stephen E. Derenzo, Edith D. Bourret-Courchesne, Nucl. Instrum. Methods A 735 (2014) 83.

[49] David N. ter Weele, Dennis R. Schaart, Pieter Dorenbos, IEEE Trans. Nucl. Sci. 61 (2014) 683.

[50] J.P. Spoonhower, M.S. Burberry, J. Lumin. 43 (1989) 221.

[51] Takao Kobayasi, Stanley Mroczkowski, James F. Owen, Lothar H. Brixner, J. Lumin. 21 (1980) 247.

[52] Mikhail S. Alekhin, Daniel A. Biner, Karl W. Krämer, Pieter Dorenbos, J. Lumin. 145 (2014) 723.

[53] Daniel Rutstrom, Luis Stand, Merry Koschan, Charles L. Melcher, Mariya Zhuravleva, J. Lumin. 216 (2019) 116740.

[54] Benjamin W. Sturm, Nerine J. Cherepy, Owen B. Drury, Peter A. Thelin, Scott E. Fisher, Sean P. O'Neal, Stephen A. Payne, Arnold Burger, Lynn A. Boatner, Joanne O. Ramey, Kanai S. Shah, Rastgo Hawrami, IEEE Nucl. Sci. Conf. R. (2011) 7.

[55] Mikhail S. Alekhin, Karl W. Krämer, Pieter Dorenbos, Nucl. Instrum. Methods A 714 (2013) 13.

[56] Yasuhiro Shoji, Shunsuke Kurosawa, Yuui Yokota, Shoki Hayasaka, Kei Kamada, Masao Yoshino, Akihiro Yamaji, Valery Chani, Yuji Ohashi, Shiro Sakuragi, Akira Yoshikawa, Cryst. Growth Des. 18 (2018) 3747.

[57] Aleksander Zych, Matthijs de Lange, Celso de Mello Donegá, Andries Meijerink, J. Appl. Phys. 112 (2012) 013536.

[58] Vesselin Dimitrov, Takayuki Komatsu, J. Solid State Chem. 196 (2012) 574.

[59] A. Feldman, D. Horowitz, R.M. Walker, M.J. Dodge, Optical Materials Characterization Final Technical Report, February 1 1978-September 30 1978. NBS Technical Note 993, 1979.

[60] J.D. Axe, G.D. Pettit, J. Phys. Chem. Solids 27 (1966) 621.

[61] Shohei Kodama, Shunsuke Kurosawa, Maki Ohno, Akihiro Yamaji, Masao Yoshino, Jan Pejchal, Robert Král, Yuji Ohashi, Kei Kamada, Yuui Yokota, Martin Nikl, Akira Yoshikawa, Radiat. Meas. 124 (2019) 54.

[62] Shohei Kodama, Shunsuke Kurosawa, Kotaro Fujii, Masatomo Yashima, Akihiro Yamaji, Akira Yoshikawa, J. Alloy. Compd. 970 (2024) 172506.